Supplementary Information

for

Tailoring high-performance bipolar membrane for durable pure water electrolysis

Weisheng Yu[1], Zirui Zhang[1], Fen Luo[1], Xiaojiang Li[1], Fanglin Duan[1], Yan Xu[1], Zhiru Liu[1], Xian Liang[1], Yaoming Wang[1], Liang Wu[1,*] & Tongwen Xu[1,*]

[1] Key Laboratory of Precision and Intelligent Chemistry, Department of Applied Chemistry, School of Chemistry and Materials Science, University of Science and Technology of China, Hefei 230026, China.

E-mail: liangwu8@ustc.edu.cn (L.W.), twxu@ustc.edu.cn (T.X.)

Table of Contents

Supplementary Notes

Model description

A 1-D isothermal multiple-physical model was performed to describe the water dissociation reactions and electrical fields produced at the CEL/AEL interface[1,2]. The schematic for the modeling domains is shown in Supplementary Fig. 2. The modeling domains comprise two electrolyte boundary layers with 10 μm thickness, an anion exchange membrane layer (AEL) and a cation exchange membrane layer (CEL) with 5, 10, or 20 μm thicknesses, an AEL|CEL junction layer with 10 nm thickness. Supplementary Tables S1 and S2 provide the relevant model parameters and equations, respectively.

Supplementary Table 1. Modeling parameters

Parameter	Description	Value
L_{mem}	Membrane thickness	4.9, 9.9, 19.9 (μm)
L_{sdl}	Diffusion boundary	10 (μm)
c_0	Initial concentration	0.5 (mol L^{-1})
Φ_0	Initial cell voltage	0 (V)
c_{fixCEM}	CEM Membrane fix charge	2.0, 1.5 (kmol m^{-3})
c_{fixAEM}	AEM Membrane fix charge	2.0, 1.5 (kmol m^{-3})
Kw_0	Water dissociation constant at zero	10.64×10^{-14} (m^3 s^{-1} mol^{-1})
Kw_r	Backward rate constant water dissociation	5.20×10^{11} (m^3 s^{-1} mol^{-1})
T	Temperature	298.15 K
A	Wien effect coefficient	0.5 (K^2 m V^{-1})
eps_r	Permitivity	78
D_H	Diffusivity	9.31×10^{-5} (cm^2 s^{-1})
D_{OH}	Diffusivity	5.26×10^{-5} (cm^2 s^{-1})
D_{Na}	Diffusivity	1.33×10^{-5} (cm^2 s^{-1})
D_{SO_4}	Diffusivity	1.07×10^{-5} (cm^2 s^{-1})
ε	Electrolyte volume fraction	1

Supplementary Table 2: Summary of governing equations.

Electric field	$E = -d(phil, x)$
Forward rate constant (kw_f)	$kw_f = Kw \times kw_r$
Bessel function (Kw)	$Kw = Kw_0 \times max(besselj(1, (2 \times sqrt(2 \times b) \times i))/(i \times sqrt(max(b, eps))), 1) \times sqrt(1/2)$
Reaction rate (rw)	$rw = Kw_f - Kw_r \times max(c_{OH}, eps^2) \times max(c_H, eps^2)$
Help variable (b)	$b = max(A \times abs(E)/eps_r/T^2, eps)$

Supplementary Figures

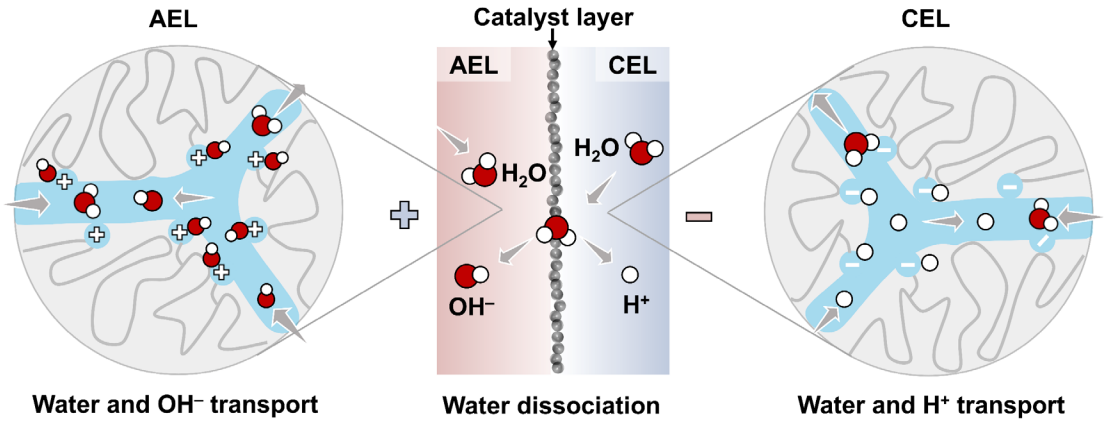

Supplementary Fig. 1 Schematic illumination of the water dissociation at the BPM interface layer and ion and water transport within the monopolar membrane layers (indicated by different colors). Under reverse bias (with AEL and CEL facing the anode and cathode, respectively), OH^- and H^+ are generated by water dissociation at the AEL|CEL interfacial layer and migrate outward through the monopolar membrane layers, while water permeates through the monopolar membrane layers and replenishes into the interfacial layer under the osmotic drive.

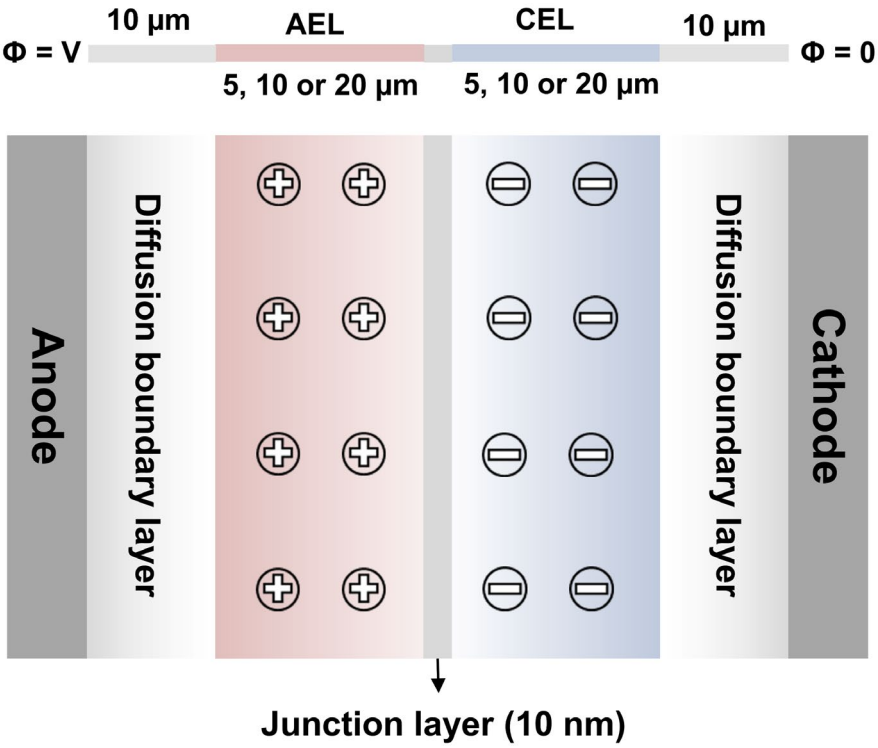

Supplementary Fig. 2 The simulated 1-D multiple-physical model is presented, which includes an AEL (5 ~ 20 μm), a CEL (5 ~ 20 μm), and a junction layer (10 nm) with two additional diffusion boundary layers (10 μm).

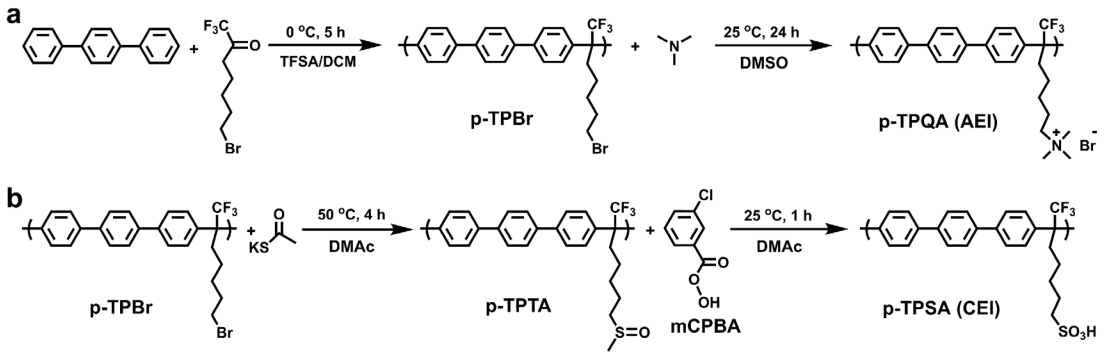

Supplementary Fig. 3 Synthesis routes of the anion- and cation exchange ionomers. (a) Synthetic pathways to bromoalkyl-tethered precursor polymer (p-TPBr) and quaternary ammonium-tethered anion exchange ionomer (p-TPQA). (b) Synthetic pathways to sulfonate-tethered proton exchange ionomer (p-TPSA).

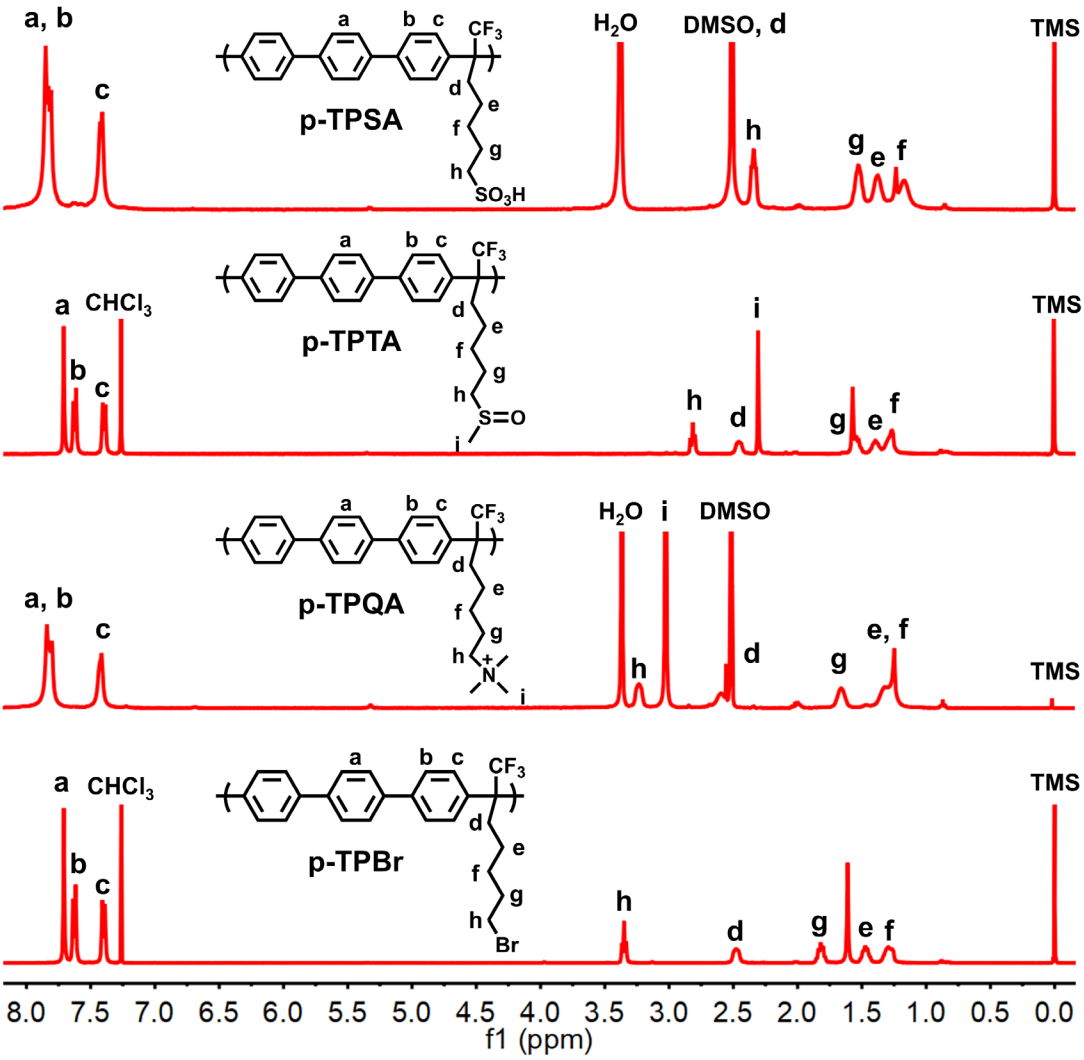

Supplementary Fig. 4 ^{1}H NMR spectra of the ionomers (p-TPSA and p-TPQA) and polymer precursors (p-TPBr and p-TPTA).

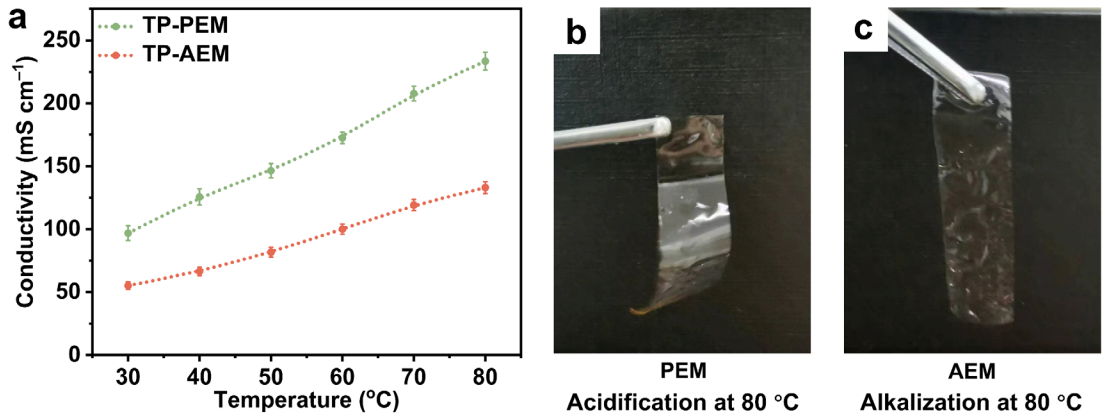

Supplementary Fig. 5 Ionic conductivity of the monopolar ion exchange membranes. (a) Proton and hydroxide conductivities of the cation (light green) and anion exchange membranes (orange). The error bars represent standard deviations over at least three tests. Photographs of the (b) cation exchange membrane and (c) anion exchange membrane. Source data are provided as a Source Data file.

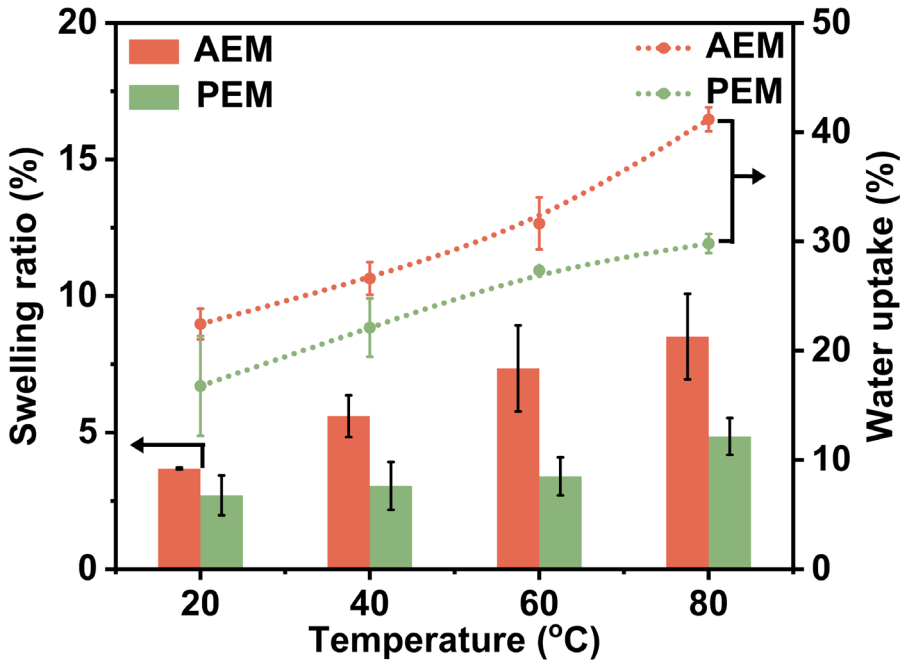

Supplementary Fig. 6 Swelling ratio and water uptake of the AEMs (orange) and PEMs (light green) at different temperatures (20 ~ 80 °C). The error bars represent standard deviations over at least three tests. Source data are provided as a Source Data file.

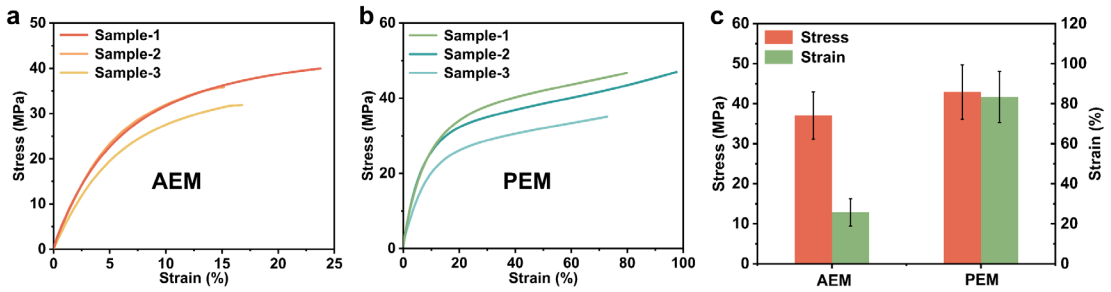

Supplementary Fig. 7 Mechanical properties of the monopolar ion exchange membranes. Stress–strain curves of the (a) anion exchange membranes and (b) cation exchange membranes. (c) Tensile strength (orange) and elongation at the break (light green) of the monopolar ion exchange membranes. The error bars represent standard deviations over at least three tests. Source data are provided as a Source Data file.

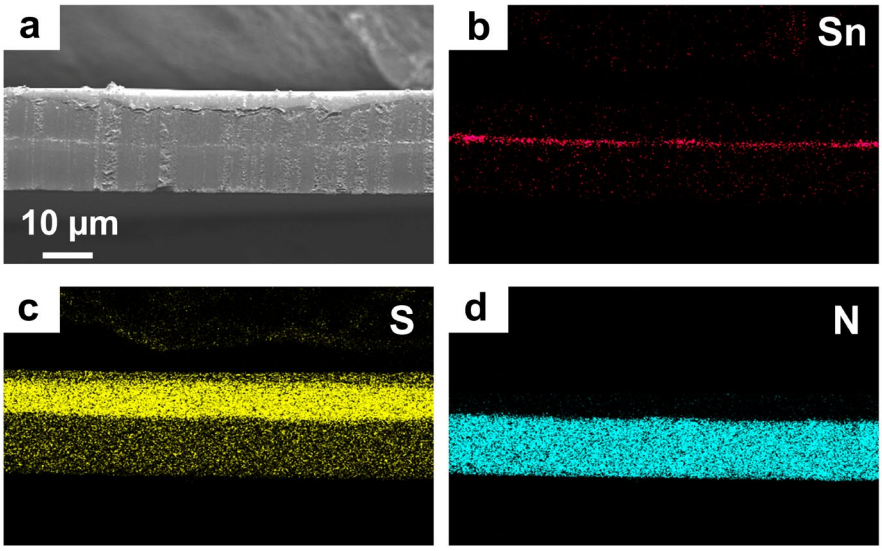

Supplementary Fig. 8 Morphology characterization of the BPM. (a) SEM cross-sectional image and (b–d) elemental mappings of the TPSn-BM before the long-term water dissociation operation.

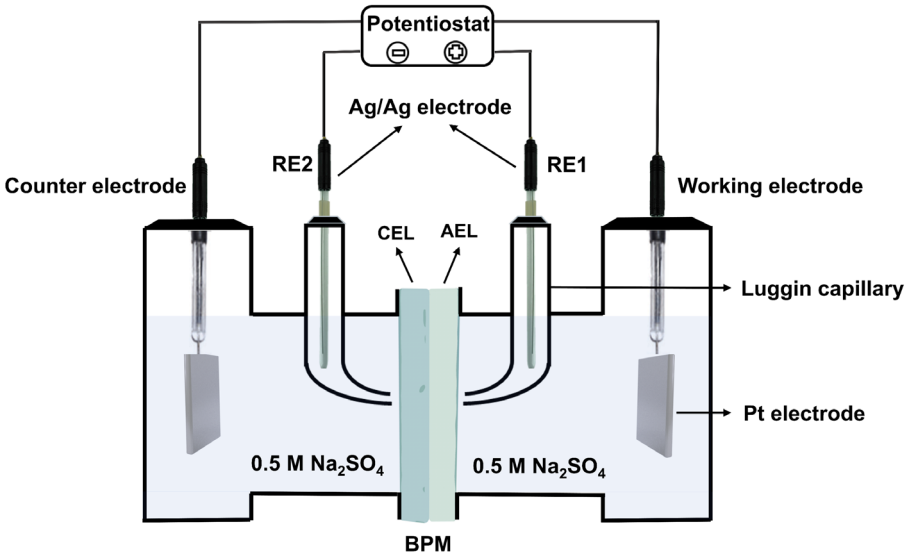

Supplementary Fig. 9 Schematic illumination of the custom-made four-electrode setup for *I*–*V* and EIS measurements. During the electrochemical measurements, the BPMs were stuck in the middle of two symmetrical compartments with an effective area of 3.14 cm^2, both the two compartments filled with 0.5 mol L^{-1} aq. Na_2SO_4. Two Pt electrodes placed outboard act as working electrode and counter electrode. Two reference electrodes (Ag/AgCl) were respectively placed inside the Luggin capillary that contacts the surface of BPMs. During long-term operation, electrolytes of both sides were fully circulated and refreshed to minimize the effects of polarization.

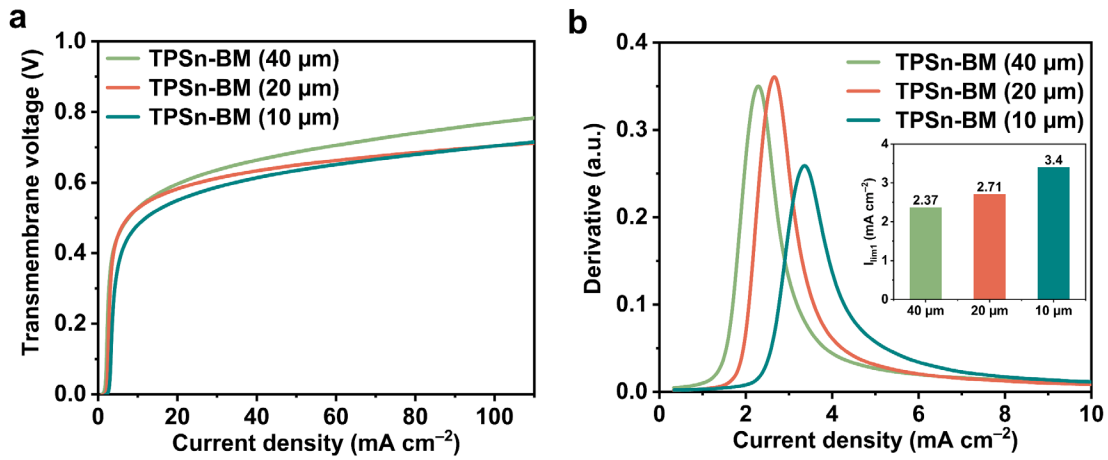

Supplementary Fig. 10 Water dissociation performance of the TPSn-BMs. (a) *I*–*V* (at current densities of 0 ~ 100 mA cm^{-2}) and (b) the corresponding derivative curves of the TPSn-BMs with different thicknesses (dark cyan, light green, and orange represent 40, 20, and 10 μm, respectively). Source data are provided as a Source Data file.

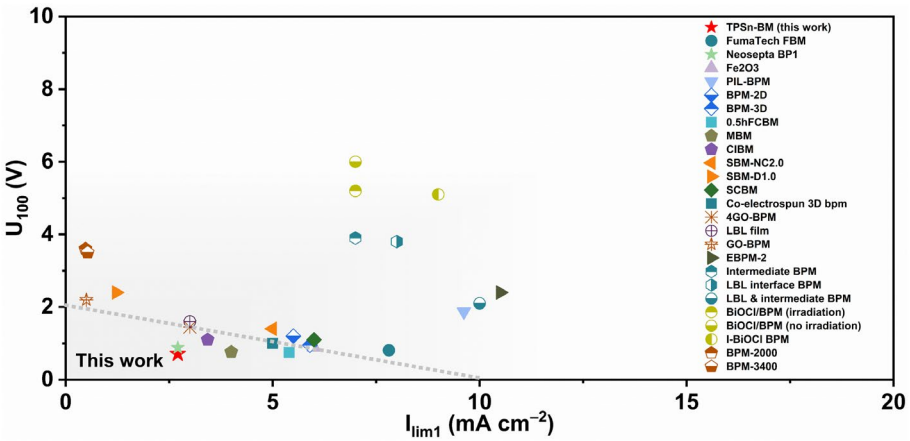

Supplementary Fig. 11 Comparison of the U_{100} and I_{lim1} values between the TPSn-BM and previously reported BPMs.

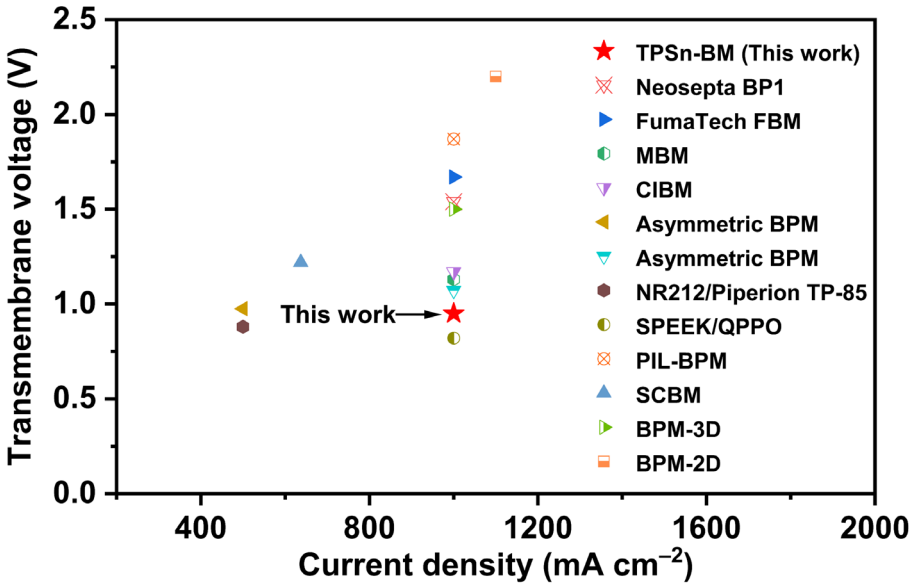

Supplementary Fig. 12 Comparison of the transmembrane voltage between the TPSn-BM and previously reported BPMs at relatively high current densities (≥ 400 mA cm^{-2}).

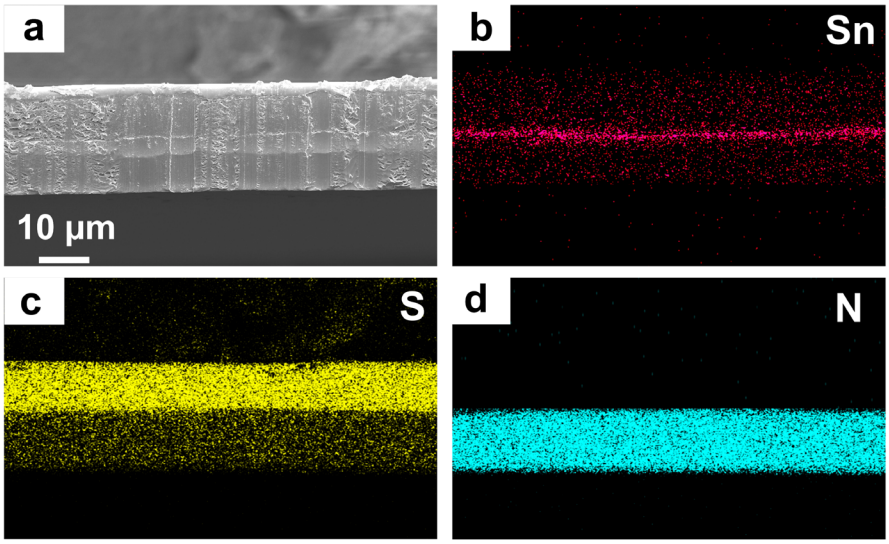

Supplementary Fig. 13 Morphology characterization of the BPM. (a) SEM cross-sectional image and (b–d) elemental mappings of the TPSn-BM after the long-term water dissociation operation.

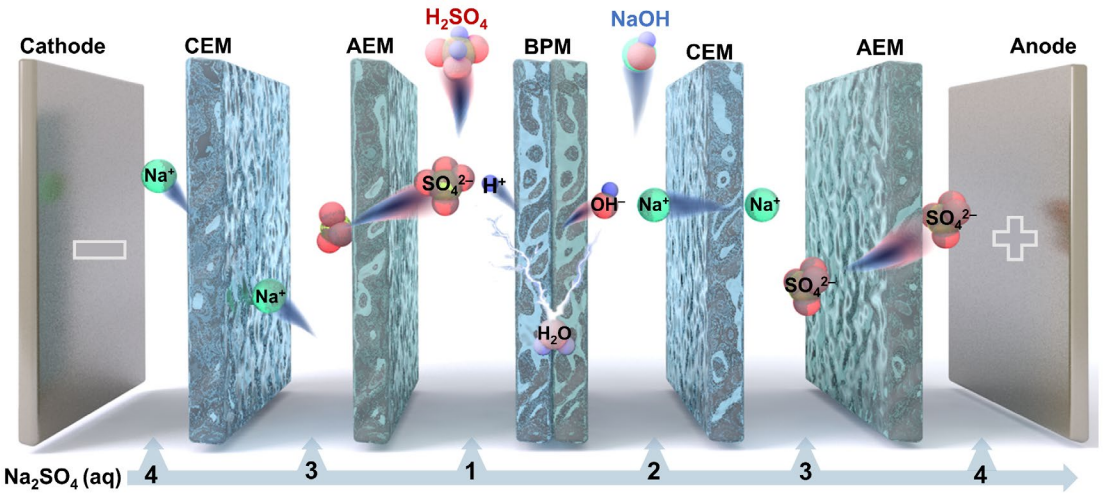

Supplementary Fig. 14 Schematic illumination of the BPM electrodialysis six-compartment setup. The BPM was placed at the center of the setup, with the CEL orientated facing the anode and the AEL facing the cathode. At a current density of 100 mA cm^{-2} (a typical value for industrial BPM-integrated applications), the generated H^+/OH^- fluxes move out from the BPM catalytic interface layer and combine with the salt ions ($SO4^{2-}$/Na^+) at the acid/base compartments for producing H_2SO_4 and NaOH, respectively.

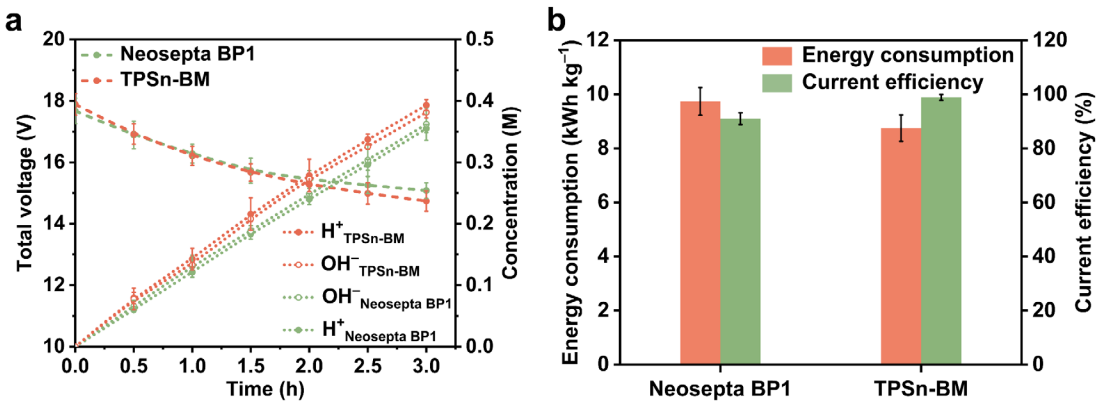

Supplementary Fig. 15 *In-situ* acid–base generation performance of the TPSn-BM and commercial Neosepta BP1. (a) The electrodialysis cell voltage and concentrations of acid (solid circle) and base (hollow circle) versus operating time. Orange and light green represent the TPSn-BM and Neosepta BP1, respectively. The error bars represent standard deviations over at least three tests. (b) The energy consumption (orange) and current efficiency (light green) of the electrodialysis cells equipped with TPSn-BM and commercial Neosepta BP1. The error bars represent standard deviations over at least three tests. Source data are provided as a Source Data file.

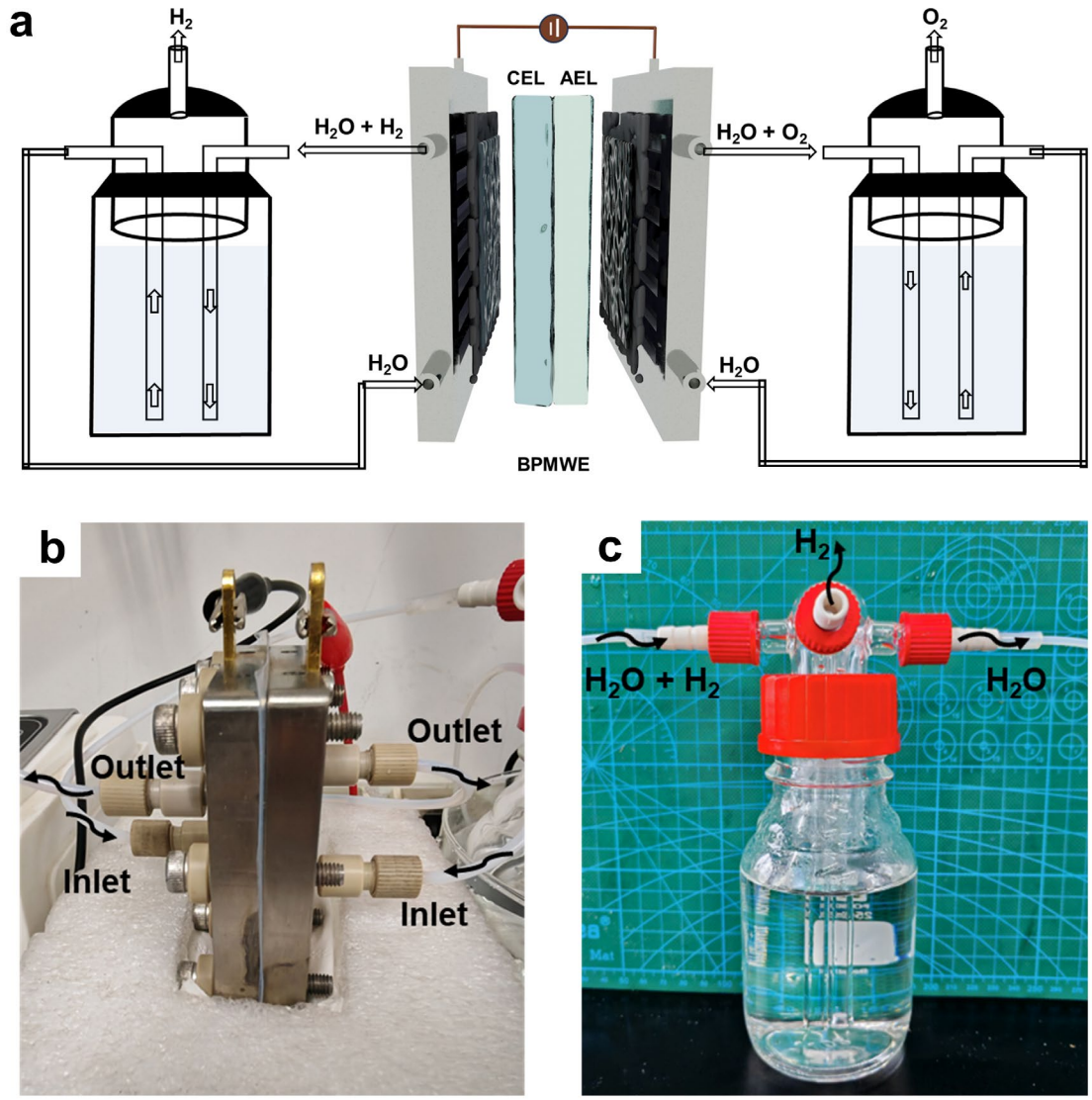

Supplementary Fig. 16 The BPM flow-cell water electrolyzer setup. (a) Schematic illumination of the pure water electrolyzer, which was composed of two Ti flow fields as the endplates and current collectors, two gaskets, two gas diffusion layers, and a BMEA equipped with a reverse bias configuration (the AEL and CEL face cathode and anode). The pure water (60 °C) is supplied to the cathode and anode through a double-channel peristaltic pump, and the generated H_2 (cathode) and O_2 (anode) are collected via a double inlet buffer bottle. (b) Photography description of the flow-cell water electrolyzer. (c) Photography description of the double inlet buffer bottle for gas collection.

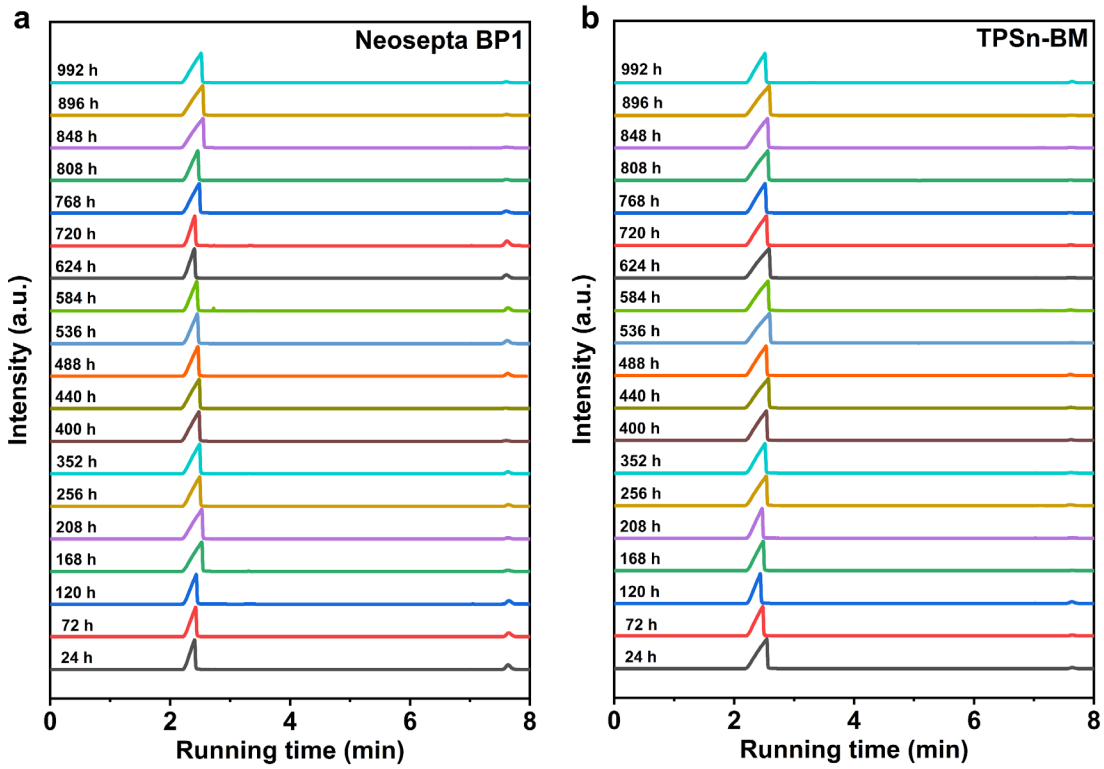

Supplementary Fig.17 Gas chromatograms of the BPM water electrolyzer cathode products versus operating time. The gas chromatograms of the water electrolyzers equipped with (a) Neosepta BP1 and (b) TPSn-BM. Source data are provided as a Source Data file.

Supplementary Tables

Supplementary Table 3 Comparison of BPM water dissociation performance.

Sample	I_{lim1} (mA cm^{-2})	U_{100} (V)	Ref.
TPSn-BM	2.71	0.71	This work
FumaTech FBM	7.81	0.81	Commercial
Neosepta BP1	2.71	0.88	Commercial
Fe_2O_3@GO	–	0.89	Ref. 3
PIL-BPM	9.62	1.87	Ref. 4
BPM-2D	5.5	1.2	Ref. 5
BPM-3D	5.9	0.95	Ref. 5
0.5hFCBM	5.4	0.75	Ref. 6
MBM	4	0.76	Ref. 7
CIBM	3.43	1.1	Ref. 8
SBM-NC2.0	5	1.4	Ref. 9
SBM-D1.0	1.22	2.4	Ref. 9
SCBM	6	1.1	Ref. 10
Fe(III)@PEI BPM	25	1.8	Ref. 11
Co-electrospun 3D bpm	5	1	Ref. 12
4GO-BPM	3	1.45	Ref. 13
LBL film	3	1.6	Ref. 14
GO-BPM	0.5	2.2	Ref. 15
MIL 101-BPM	19	4.2	Ref. 16
EBPM-2	10.5	2.4	Ref. 17
Intermediate BPM	7	3.9	Ref. 18
LBL interface BPM	8	3.8	Ref. 18
LBL & intermediate BPM	10	2.1	Ref. 18
BiOCl/BPM (irradiation)	7	5.2	Ref. 19
BiOCl/BPM (no irradiation)	7	6	Ref. 19
I-BiOCl BPM	9	5.1	Ref. 19
BPM-ZrOH	0.424	9	Ref. 20
BPM-SiOH	0.5	10	Ref. 20
BPM-TiOH	0.46	12	Ref. 20
BPM-2000	0.48	3.6	Ref. 21
BPM-3400	0.53	3.5	Ref. 21

Supplementary Table 4 Comparison of BPM electrolyzer performance and stability.

BPM-based application	Current density ($mA\ cm^{-2}$)	Operating time (h)	Temperature (°C)	Ref.
Water electrolysis	300 ~ 500	1000	60	This
Water electrolysis (Acid-base feed)	20	12	25	Ref. 22
Water electrolysis	500	–	60	Ref. 23
Water electrolysis (Bipolar interface)	400	500	80	Ref. 24
Water electrolysis	1000	4	50	Ref. 25
Water electrolysis	500	–	50	Ref. 26
Water electrolysis	500	~ 60	55	Ref. 27
Ammonia electrosynthesis	1000	110	–	Ref. 7
Ammonia electrosynthesis	1000	210	–	Ref. 8
CO_2 electrolysis	100	2.5	–	Ref. 28
CO_2 electrolysis	300	25	–	Ref. 29
CO_2 electrolysis	150	145	–	Ref. 30
CO_2 electrolysis	300	14	–	Ref. 31
CO_2 electrolysis	150	11	–	Ref. 32

Supplementary References

1. Bui, J. C., Digdaya, I., Xiang, C., Bell, A. T. & Weber, A. Z. Understanding multi-ion transport mechanisms in bipolar membranes. *ACS Appl. Mater. Interfaces* **12**, 52509–52526 (2020).
2. Zhang, H., Cheng, D., Xiang, C. & Lin, M. Tuning the interfacial electrical field of bipolar membranes with temperature and electrolyte concentration for enhanced water dissociation. *ACS Sustainable Chem. Eng.* **11**, 8044–8054 (2023).
3. Kim, B. S. *et al.* Bipolar membranes to promote formation of tight ice-like water for efficient and sustainable water splitting. *Small* **16**, 2002641 (2020).
4. Li, G. *et al.* In-situ grown polyaniline catalytic interfacial layer improves water dissociation in bipolar membranes. *Sep. Purif. Technol.* **275**, 119167 (2021).
5. Shen, C., Wycisk, R. & Pintauro, P. N. High performance electrospun bipolar membrane with a 3D junction. *Energy Environ. Sci.* **10**, 1435–1442 (2017).
6. Ge, Z. *et al.* High-performance bipolar membrane for electrochemical water electrolysis. *J. Membr. Sci.* **656**, 120660 (2022).
7. Xu, Z. *et al.* Continuous ammonia electrosynthesis using physically interlocked bipolar membrane at 1000 mA cm^{-2}. *Nat. Commun.* **14**, 1619 (2023).
8. Xu, Z. *et al.* A chemically interlocked bipolar membrane achieving stable water dissociation for high output ammonia electrosynthesis. *Energy Environ. Sci.* **16**, 3815–3824 (2023).
9. Eswaraswamy, B., Suhag, A., Goel, P., Mandal, P. & Chattopadhyay, S. Potential of montmorillonite nanoclay as water dissociation catalyst at the interface of bipolar membrane. *Sep. Purif. Technol.* **295**, 121257 (2022).
10. Shehzad, M. A. *et al.* Shielded goethite catalyst that enables fast water dissociation in bipolar membranes. *Nat. Commun.* **12**, 9 (2021).
11. Ge, Z. *et al.* Beneficial use of a coordination complex as the junction catalyst in a bipolar membrane. *ACS Appl. Energy Mater.* **3**, 5765–5773 (2020).
12. Chen, Y. *et al.* High-performance bipolar membrane development for improved water dissociation. *ACS Appl. Polym. Mater.* **2**, 4559–4569 (2020).

13. Yan, Z. *et al.* The balance of electric field and interfacial catalysis in promoting water dissociation in bipolar membranes. *Energy Environ. Sci.* **11**, 2235–2245 (2018).
14. McDonald, M. B., Freund, M. S. & Hammond, P. T. Catalytic, Conductive bipolar membrane interfaces through layer-by-layer deposition for the design of membrane-integrated artificial photosynthesis systems. *ChemSusChem* **10**, 4599–4609 (2017).
15. McDonald, M. B., Bruce, J. P., McEleney, K. & Freund, M. S. Reduced graphene oxide bipolar membranes for integrated solar water splitting in optimal pH. *ChemSusChem* **8**, 2645–2654 (2015).
16. Wang, Q., Wu, B., Jiang, C., Wang, Y. & Xu, T. Improving the water dissociation efficiency in a bipolar membrane with amino-functionalized MIL-101. *J. Membr. Sci.* **524**, 370–376 (2017).
17. Pan, J. *et al.* Preparation of bipolar membranes by electrospinning. *Mater. Chem. Phys.* **186**, 484–491 (2017).
18. Abdu, S. *et al.* Catalytic polyelectrolyte multilayers at the bipolar membrane interface. *ACS Appl. Mater. Interfaces* **5**, 10445–10455 (2013).
19. Liu, X., Yang, H., Dai, H., Mao, X. & Liang, Z. A novel photoelectrocatalytic approach for water splitting by an I-BiOCl/bipolar membrane sandwich structure. *Green Chem.* **17**, 199–203 (2015).
20. Rajesh, A. M., Chakrabarty, T., Prakash, S. & Shahi, V. K. Effects of metal alkoxides on electro-assisted water dissociation across bipolar membranes. *Electrochim. Acta* **66**, 325–331 (2012).
21. Rajesh, A. M., Kumar, M. & Shahi, V. K. Functionalized biopolymer based bipolar membrane with poly ethylene glycol interfacial layer for improved water splitting. *J. Membr. Sci.* **372**, 249–257 (2011).
22. Lee, L. & Kim, D. Poly(arylene ether ketone)-based bipolar membranes for acid–alkaline water electrolysis applications. *J. Mater. Chem. A* **9**, 5485–5496 (2021).
23. Chen, L., Xu, Q., Oener, S. Z., Fabrizio, K. & Boettcher, S. W. Design principles for water dissociation catalysts in high-performance bipolar membranes. *Nat. Commun.* **13**, 3846 (2022).

24. Tricker, A. W. *et al.* Engineering bipolar interfaces for water electrolysis using earth-abundant anodes. *ACS Energy Lett.* **8**, 527–5280 (2023).
25. Oener, S. Z., Twight, L. P., Lindquist, G. A. & Boettcher, S. W. Thin cation-exchange layers enable high-current-density bipolar membrane electrolyzers via improved water transport. *ACS Energy Lett.* **6**, 1–8 (2020).
26. Oener, S. Z., Foster, M. J. & Boettcher, S. W. Accelerating water dissociation in bipolar membranes and for electrocatalysis. *Science* **369**, 1099–1103 (2020).
27. Kao, Y. L., Chen, L., Boettcher, S. W. & Aili, D. Divergent synthesis of bipolar membranes combining strong interfacial adhesion and high-rate capability. *ACS Energy Lett.* **9**, 2953−2959 (2024).
28. Li, T. *et al.* Electrolytic conversion of bicarbonate into CO in a Flow Cell. *Joule* **3**, 1487–1497 (2019).
29. Lee, G. *et al.* CO_2 electroreduction to multicarbon products from carbonate capture liquid. *Joule* **7**, 1277–1288 (2023).
30. Li, Y. C. *et al.* CO_2 Electroreduction from carbonate electrolyte. *ACS Energy Lett.* **4**, 1427–1431 (2019).
31. Alkayyali, T. *et al.* Direct membrane deposition for CO_2 Electrolysis. *ACS Energy Lett.* **8**, 4674–4683 (2023).
32. Chen, Y. *et al.* A robust, scalable platform for the electrochemical conversion of CO_2 to formate: Identifying pathways to higher energy efficiencies. *ACS Energy Lett.* **5**, 1825–1833 (2020).